Atomic imaging of the edge structure and growth of a two-dimensional hexagonal ice

https://doi.org/10.1038/s41586-019-1853-4

Received: 3 March 2019

Accepted: 19 September 2019

Published online: 1 January 2020

Runze Ma[1,2,14], Duanyun Cao[1,14], Chongqin Zhu[3,4,14], Ye Tian[1,14], Jinbo Peng[1], Jing Guo[1], Ji Chen[5], Xin-Zheng Li[5,6], Joseph S. Francisco[3], Xiao Cheng Zeng[4,7,8,9,10]*, Li-Mei Xu[1,6]*, En-Ge Wang[1,11,12]* & Ying Jiang[1,6,13]*

The formation and growth of water-ice layers on surfaces and of low-dimensional ice under confinement are frequent occurrences[1–4]. This is exemplified by the extensive reporting of two-dimensional (2D) ice on metals[5–11], insulating surfaces[12–16], graphite and graphene[17,18] and under strong confinement[14,19–22]. Although structured water adlayers and 2D ice have been imaged, capturing the metastable or intermediate edge structures involved in the 2D ice growth, which could reveal the underlying growth mechanisms, is extremely challenging, owing to the fragility and short lifetime of those edge structures. Here we show that noncontact atomic-force microscopy with a CO-terminated tip (used previously to image interfacial water with minimal perturbation)[12], enables real-space imaging of the edge structures of 2D bilayer hexagonal ice grown on a Au(111) surface. We find that armchair-type edges coexist with the zigzag edges usually observed in 2D hexagonal crystals, and freeze these samples during growth to identify the intermediate edge structures. Combined with simulations, these experiments enable us to reconstruct the growth processes that, in the case of the zigzag edge, involve the addition of water molecules to the existing edge and a collective bridging mechanism. Armchair edge growth, by contrast, involves local seeding and edge reconstruction and thus contrasts with conventional views regarding the growth of bilayer hexagonal ices and 2D hexagonal matter in general.

Scanning tunnelling microscopy (STM) has been widely used to study 2D ices at surfaces[7,9,10], but resolving edge structures is difficult because STM is not sensitive to the position of nuclei and its tip can induce disturbances. Although transmission electron microscopy (TEM) can resolve atomic lattice edges[23], high-resolution TEM usually requires high-energy electrons that can change or even completely decompose the edge structure of covalently bonded 2D materials[23] and are expected to damage more weakly bonded ice edges. By contrast, noncontact atomic-force microscopy (AFM) based on a qPlus sensor[24,25] can probe interfacial water with excellent resolution[12,26,27], with use of a CO-terminated tip ensuring that water molecules are only minimally disturbed thanks to the ultrahigh flexibility of the tip apex and the weak higher-order electrostatic force[12]. Here we use this method to image various metastable edge structures of a 2D bilayer hexagonal ice grown on a Au(111) surface (Fig. 1a) and resolve the growth mechanisms with atomic detail.

The 2D ice was grown on a Au(111) surface at about 120 K with a thickness of around 2.5 Å (see Methods, Fig. 1a), corresponding to two water overlayers (Extended Data Fig. 1a–f). The STM image of the 2D ice (Fig. 1c) and the corresponding fast Fourier transform (FFT) image (inset of Fig. 1a) both show a well ordered hexagonal structure, with periodicity[6] Au(111)-$\sqrt{3} \times \sqrt{3}$-30° (Wood's notation; Extended Data Fig. 1g). Although the honeycomb H-bonding network of the 2D ice is visible in the STM image, the detailed topology of the edge structures is difficult to resolve. The AFM frequency-shift (Δf) image of the same island exhibits much higher resolution (Fig. 1d), such that the atomic structures of the zigzag and armchair edges can be easily identified. The total length of the zigzag and the armchair edges are comparable, but the average length of the former is statistically somewhat larger (two-sided t-test, $P = 1 \times 10^{-7}$; Fig. 1b). Zigzag edges can grow perfectly up to lengths of 60 Å, but armchair edges are always interrupted by step kinks or defects that result in shorter lengths, predominantly around 10–30 Å (Extended Data Fig. 2).

We then performed systematic AFM imaging at different tip heights (see Methods and Fig. 2a). At a large tip height, where the AFM signals are dominated by the higher-order electrostatic force[12], we can distinguish two sets of $\sqrt{3} \times \sqrt{3}$ sub-lattices in the 2D bilayer ice, one of which

[1]International Center for Quantum Materials, School of Physics, Peking University, Beijing, China. [2]Physical Science Laboratory, Huairou National Comprehensive Science Centre, Beijing, China. [3]Department of Earth and Environmental Science, University of Pennsylvania, Philadelphia, PA, USA. [4]Department of Chemistry, University of Nebraska–Lincoln, Lincoln, NE, USA. [5]School of Physics, Peking University, Beijing, China. [6]Collaborative Innovation Center of Quantum Matter, Beijing, China. [7]Department of Chemical and Biomolecular Engineering, University of Nebraska–Lincoln, Lincoln, NE, USA. [8]Department of Mechanical & Materials Engineering, University of Nebraska–Lincoln, Lincoln, NE, USA. [9]Department of Physics, University of Nebraska–Lincoln, Lincoln, NE, USA. [10]Nebraska Center for Materials and Nanoscience, University of Nebraska–Lincoln, Lincoln, NE, USA. [11]Ceramics Division, Songshan Lake Materials Lab, Institute of Physics, Chinese Academy of Sciences, Guangdong, China. [12]School of Physics, Liaoning University, Shenyang, China. [13]CAS Center for Excellence in Topological Quantum Computation, University of Chinese Academy of Sciences, Beijing, China. [14]These authors contributed equally: Runze Ma, Duanyun Cao, Chongqin Zhu, Ye Tian. *e-mail: xzeng1@unl.edu; limei.xu@pku.edu.cn; egwang@pku.edu.cn; yjiang@pku.edu.cn

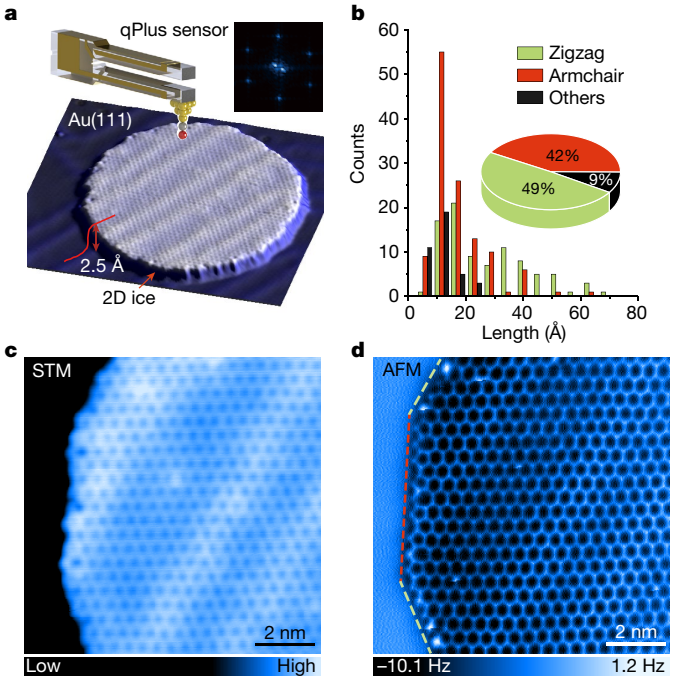

Fig. 1 | Experimental setup and STM and AFM images of 2D bilayer ice. **a**, Schematic of STM and AFM imaging of a 2D bilayer ice island on Au(111) using qPlus-based non-contact AFM with a CO-terminated tip. Inset, 2D FFT image inside the 2D ice island. The line profile across the step edge shows the height of the island (about 2.5 Å). **b**, Length distribution diagram of the zigzag and armchair edges for ten ice islands (n = 249). Inset, statistics on the length of the zigzag and armchair edges as a fraction of the total length of all counted edges. **c**, Constant-current STM image acquired at the set point, 100 mV and 10 pA. **d**, Constant-height AFM (Δf) image of the same area as in **c**, recorded at a tip height of 10 pm. The zigzag and armchair edges are denoted by green and red dashed lines, respectively. The tip height is referenced to the STM set point on the bilayer ice (100 mV, 50 pA), and the oscillation amplitude is 100 pm.

is highlighted in Fig. 2a (left panel). At a smaller tip height, the bright features of this sub-lattice start to show directionality, and the other sub-lattice resolves into a V-shaped feature (see the red lines in Fig. 2a, middle panel). When the tip height is further decreased to enter into the Pauli repulsion-force region, the AFM image shows a honeycomb structure with sharp lines connecting the two sub-lattices, resembling the H bonds (Fig. 2a, right panel).

Density functional theory (DFT) calculations reveal that the 2D ice grown on the Au(111) surface corresponds to an interlocked bilayer ice structure (Fig. 2c) consisting of two flat hexagonal water layers (see Methods). The hexagons of the two sheets are in registry and the angle between water molecules in the plane is 120°. In each water layer, half of the water molecules are lying flat (parallel to the substrate), and the other half are vertical (perpendicular to the substrate), with one O–H either upward or downward. The vertical water in one layer donates a H bond to the flat water in the other layer, leading to a fully saturated H-bonding structure. Although evidence for such a flat bilayer of hexagonal ice has been observed previously on hydrophobic surfaces and under hydrophobic confinements[17–19], its atomic structure has not been directly imaged.

The AFM simulation using a quadrupole (d_{z^2}) tip (Fig. 2b, Methods) based on the above model agrees well with the experimental results (Fig. 2a, Extended Data Fig. 3). The very similar height of the flat and vertical water molecules makes it very difficult to distinguish them in STM images. However, the flat and vertical water molecules show distinctly different contrast in AFM images (Fig. 2a, b, left panel) because the higher-order electrostatic force is very sensitive to the orientation of the water molecules[12,26]. We can additionally discern the O–H directionality of the flat and vertical water via the interplay between the higher-order electrostatic forces and Pauli repulsion forces (Extended Data Fig. 3), as highlighted by the red lines in Fig. 2a, b (middle panel). At small tip heights, where the Pauli repulsion force is dominant, the sharp bond-like features represent ridges of the potential-energy landscape experienced by the functionalized probe, mainly arising from the lateral relaxation of the CO tip induced by the Pauli repulsion force[28] (Fig. 2a, b, right panel).

Figure 3a, b (step 1) displays magnified AFM images of the zigzag and armchair edges, respectively, revealing that the zigzag edge grows

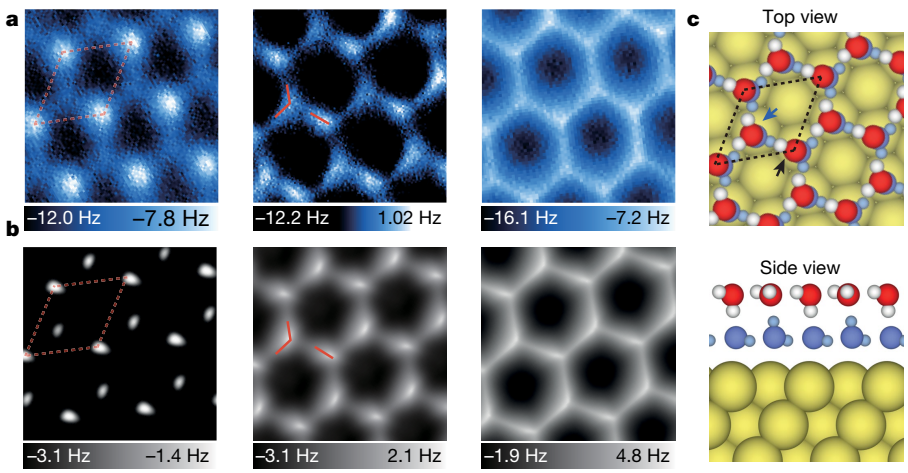

Fig. 2 | Detailed AFM characterization of the 2D bilayer ice and the corresponding structural model. **a**, Constant-height AFM (Δf) imaging at tip heights of 20 pm (left), 0 pm (middle) and −10 pm (right). **b**, Simulated AFM images at tip heights of 14 Å (left), 13.7 Å (middle) and 13.5 Å (right). The $\sqrt{3} \times \sqrt{3}$ unit cell is indicated by the dashed red rhombus. The O–H directionality of the water molecules is highlighted by the solid red lines. **c**, Top and side views of the bilayer ice structure on the Au(111) surface. Au, H and O atoms in the top water layer are denoted as yellow, white and red spheres, respectively. H and O atoms in the bottom water layer are shown by blue spheres (with a smaller size for clarity). The flat and vertical water molecules in the top layer are denoted by the blue and black arrows, respectively. In the side view, only the water molecules along one zigzag direction are shown for a clearer view of the top–bottom water pairs. The tip heights in **a** are referenced to the STM set point on the bilayer ice (100 mV, 50 pA). The tip heights in **b** are defined as the vertical distance between the apex atom of the metal tip and the outermost atom of the Au substrate. All the oscillation amplitudes of the experimental and simulated images are 100 pm and the image sizes are 1.25 nm × 1.25 nm.

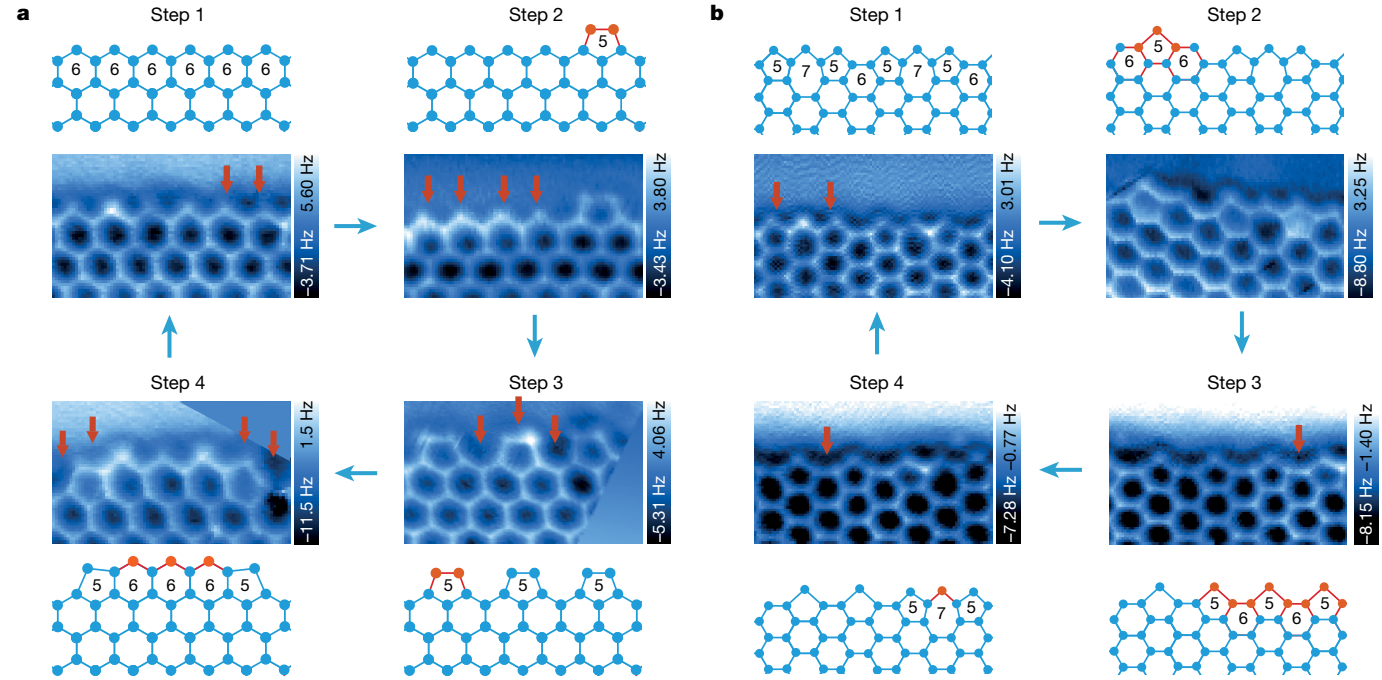

Fig. 3 | Proposed growing process for zigzag and armchair edges. **a**, **b**, Constant-height AFM images and the corresponding ball-and-stick models of the most stable (1) and metastable structures (2–4) of zigzag (**a**) and armchair (**b**) edges. The proposed growing process cycles through steps 1 to 4. In the AFM images, each red arrow indicates the addition of one bilayer water pair, leading to the structure in the subsequent image. In the ball-and-stick models, the red balls and sticks represent the newly added bilayer water pairs, and those in blue represent the existing structures. The size of the images is 3.2 nm × 1.9 nm (**a**) and 3.7 nm × 2.2 nm (**b**).

under preservation of its original structure, but the armchair-edge growth involves edge reconstruction into a periodic structure of 5756-type member rings—that is, where the edge structure periodically repeats the sequence pentagon–heptagon–pentagon–hexagon. DFT calculations indicate that the unreconstructed zigzag edge and the 5756-type armchair edge are the most stable edges (Extended Data Fig. 4). The 5756-type armchair edge forms as a result of combined effects that minimize the number of unsaturated H bonds and reduce the strain energy (Extended Data Fig. 5). It is well known that the basal planes of hexagonal ice are usually terminated with zigzag edges and that armchair edges are absent because of the higher density of unsaturated H bonds. However, in lower-dimensional systems or under confinement, the armchair edge can lower its energy by proper reconstruction.

After ice growth was stopped at 120 K, the sample was immediately cooled down to 5 K (see Methods) in an attempt to freeze metastable or intermediate edge structures and ensure relatively long lifetimes to allow STM and AFM imaging. Owing to the weakly perturbative character of the CO-functionalized tip[12], we were able to identify metastable and intermediate structures and reconstruct the 2D ice-growing process (Fig. 3).

For zigzag edges, we occasionally find individual pentagons attached to the straight edges and that these can line up to form an array with a periodicity of $2 \times a_{ice}$ (where a_{ice} is the lattice constant of the 2D ice). We interpret this as indicating that the growth of the zigzag edges is initiated by the formation of a periodic array of pentagons (Fig. 3a, steps 1–3), which involves the addition of two water pairs for a pentagon (see red arrows). The pentagon array is then bridged to form a 56665-type structure (Fig. 3a, step 4) and eventually recovers the original zigzag edge by adding more water pairs. Interestingly, we can even capture the tip-induced growth of an individual pentagon (Extended Data Fig. 6).

By contrast, the armchair edges do not exhibit this pentagon array structure and we instead frequently observe short 5656-type steps at the edge (Extended Data Fig. 2). The length of the 5656-type edges is considerably shorter than that of the 5756-type edges, presumably

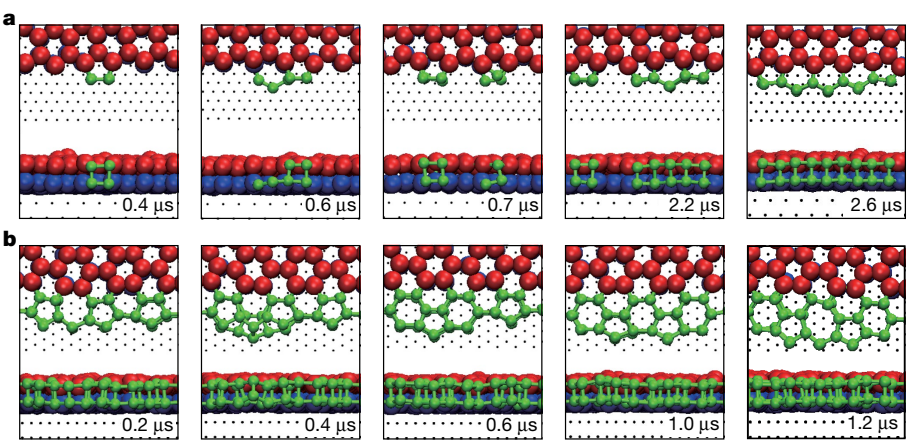

Fig. 4 | Molecular-dynamics simulation of the growth of the zigzag and armchair edges. **a**, **b**, Time-lapse snapshots of molecular-dynamics simulations during the growth of the zigzag (**a**) and armchair (**b**) edges. The simulation times are indicated in the bottom right of each snapshot. In all snapshots (upper panel, top view; lower panel, side view), the red and blue spheres represent the top-layer and bottom-layer water molecules of a pre-existing bilayer ice grain, respectively. The green spheres represent newly deposited water molecules and formed structures during the simulated growth process.

because the 5656-type edge is heavily stressed and is less stable than the 5756-type edge (Extended Data Fig. 5). Starting from the 5756-type armchair edge, the 575-type member rings are locally converted to 656-type member rings by the addition of two water pairs (Fig. 3b, step 2). The 656-type member rings then grow laterally to form a 5656-type edge (Fig. 3b, step 3) but with limited length, owing to the accumulation of strain energy. The strain can be partially relaxed by inserting one water pair into the hexagon of the 5656-type edge, leading again to the formation of a 5756-type edge (Fig. 3b, step 4). Kinetically, such a growth mechanism prohibits the formation of armchair edges as long as the zigzag edges (Fig. 1b).

To further corroborate this proposed growth mechanism, molecular-dynamics simulations of water vapour on a Au(111) surface were carried out (see Methods). We found that 2D bilayer ice islands form on the surface, in agreement with our experimental observations (Extended Data Figs. 7, 8). The collective bridging mechanism at the zigzag edge is perfectly reproduced in Fig. 4a. It is worth noting that the single pentagon attached to the zigzag edge cannot act as a local nucleation centre to promote the growth (t = 0.6–0.7 μs in Fig. 4a, Supplementary Video 1). Instead, a periodic but unconnected array of pentagons is initially formed at the zigzag edge, and subsequent incoming water molecules collectively attempt to connect these pentagons, resulting in a 565-chain structure (t = 2.2 μs in Fig. 4a, Supplementary Video 2). Such a structure was not observed experimentally, owing to its short lifetime (Extended Data Fig. 9). The addition of one water pair further bridges the 565-type structure and the nearby pentagon, leading to the formation of a 5666-type structure (t = 2.4 μs; see Supplementary Videos 3, 4). The 5666-type structure grows laterally to form a 56665-type structure (t = 2.6 μs) and eventually turns into a fully connected hexagon array.

As for the armchair edges, the local seeding growth can be clearly seen in Fig. 4b, agreeing nicely with the proposed mechanism from our experiments (Fig. 3b). The conversion from 575- to 656-type member rings starts from the bottom layer, forming a composite 575/656 structure (t = 0.4 μs in Fig. 4b, Supplementary Videos 5, 6), which is indistinguishable from the 5756-type edge in the experiments, because only the top layer of the 2D bilayer ice can be imaged. The resulting 656 step then serves as the nucleation centre to grow the 5656-type edge (t = 0.6–1 μs, Supplementary Video 7). The addition of one water molecule into the 5656-type edge results in a highly mobile unpaired-molecule structure (Supplementary Video 8). Two of those unpaired water molecules can subsequently coalesce into a more stable heptagon structure, completing the 5656-to-5756 conversion (t = 1.2 μs, Supplementary Video 9).

We believe that the observed growth behaviour is a generic phenomenon for 2D ice, given that the relative stability of the different edge structures shows negligible dependence on the water spacing and the commensurability with the substrate (Extended Data Fig. 10). Indeed, bilayer hexagonal ice forms on different hydrophobic surfaces[6,17,18] and under hydrophobic confinement[19,22], and can be viewed as a stand-alone 2D crystal (2D ice I), the formation of which is insensitive to the underlying structure of the substrate[29]. Although it would be exceedingly difficult to extend our imaging method to observe three-dimensional (3D) ice growth[8,30], the growth mechanism that we have uncovered might also occur at the surface of bilayer hexagonal ice, because it lacks dangling H bonds on its surface and might therefore support bilayer-on-bilayer ice growth and ultimately a 2D-to-3D ice transformation.

Online content

Any methods, additional references, Nature Research reporting summaries, source data, extended data, supplementary information, acknowledgements, peer review information; details of author contributions and competing interests; and statements of data and code availability are available at https://doi.org/10.1038/s41586-019-1853-4.

1. Cao, L. L. et al. Anti-icing superhydrophobic coatings. *Langmuir* **25**, 12444–12448 (2009).
2. Weber, B. et al. Molecular insight into the slipperiness of ice. *J. Phys. Chem. Lett.* **9**, 2838–2842 (2018).
3. Graether, S. P. et al. β-helix structure and ice-binding properties of a hyperactive antifreeze protein from an insect. *Nature* **406**, 325–328 (2000).
4. Kiselev, A. et al. Active sites in heterogeneous ice nucleation—the example of K-rich feldspars. *Science* **355**, 367–371 (2017).
5. Hodgson, A. & Haq, S. Water adsorption and the wetting of metal surfaces. *Surf. Sci. Rep.* **64**, 381–451 (2009).
6. Corem, G. et al. Ordered H_2O structures on a weakly interacting surface: a helium diffraction study of H_2O/Au(111). *J. Phys. Chem. C* **117**, 23657–23663 (2013).
7. Nie, S., Feibelman, P. J., Bartelt, N. C. & Thurmer, K. Pentagons and heptagons in the first water layer on Pt(111). *Phys. Rev. Lett.* **105**, 026102 (2010).
8. Thurmer, K. & Nie, S. Formation of hexagonal and cubic ice during low-temperature growth. *Proc. Natl Acad. Sci. USA* **110**, 11757–11762 (2013).
9. Maier, S., Lechner, B. A., Somorjai, G. A. & Salmeron, M. Growth and structure of the first layers of ice on Ru(0001) and Pt(111). *J. Am. Chem. Soc.* **138**, 3145–3151 (2016).
10. Lin, C. et al. Two-dimensional wetting of a stepped copper surface. *Phys. Rev. Lett.* **120**, 076101 (2018).
11. Mehlhorn, M. & Morgenstern, K. Faceting during the transformation of amorphous to crystalline ice. *Phys. Rev. Lett.* **99**, 246101 (2007).
12. Peng, J. B. et al. Weakly perturbative imaging of interfacial water with submolecular resolution by atomic force microscopy. *Nat. Commun.* **9**, 122 (2018).
13. Hu, J., Xiao, X. D., Ogletree, D. F. & Salmeron, M. Imaging the condensation and evaporation of molecularly thin-films of water with nanometer resolution. *Science* **268**, 267–269 (1995).
14. Xu, K., Cao, P. G. & Heath, J. R. Graphene visualizes the first water adlayers on mica at ambient conditions. *Science* **329**, 1188–1191 (2010).
15. Odelius, M., Bernasconi, M. & Parrinello, M. Two dimensional ice adsorbed on mica surface. *Phys. Rev. Lett.* **78**, 2855–2858 (1997).
16. Meier, M. et al. Water agglomerates on Fe_3O_4(001). *Proc. Natl Acad. Sci. USA* **115**, E5642–E5650 (2018).
17. Lupi, L., Kastelowitz, N. & Molinero, V. Vapor deposition of water on graphitic surfaces: formation of amorphous ice, bilayer ice, ice I, and liquid water. *J. Chem. Phys.* **141**, 18C508 (2014).
18. Kimmel, G. A. et al. No confinement needed: observation of a metastable hydrophobic wetting two-layer ice on graphene. *J. Am. Chem. Soc.* **131**, 12838–12844 (2009).
19. Koga, K., Zeng, X. C. & Tanaka, H. Freezing of confined water: a bilayer ice phase in hydrophobic nanopores. *Phys. Rev. Lett.* **79**, 5262–5265 (1997).
20. Algara-Siller, G. et al. Square ice in graphene nanocapillaries. *Nature* **519**, 443–445 (2015).
21. Chen, J. et al. Two-dimensional ice from first principles: structures and phase transitions. *Phys. Rev. Lett.* **116**, 025501 (2016).
22. Bampoulis, P. et al. Hydrophobic ice confined between graphene and MoS_2. *J. Phys. Chem. C* **120**, 27079–27084 (2016).
23. Girit, C. O. et al. Graphene at the edge: stability and dynamics. *Science* **323**, 1705–1708 (2009).
24. Giessibl, F. J. Advances in atomic force microscopy. *Rev. Mod. Phys.* **75**, 949–983 (2003).
25. Gross, L. et al. The chemical structure of a molecule resolved by atomic force microscopy. *Science* **325**, 1110–1114 (2009).
26. Peng, J. B. et al. The effect of hydration number on the interfacial transport of sodium ions. *Nature* **557**, 701–705 (2018).
27. Shiotari, A. & Sugimoto, Y. Ultrahigh-resolution imaging of water networks by atomic force microscopy. *Nat. Commun.* **8**, 14313 (2017).
28. Hapala, P. et al. Mechanism of high-resolution STM/AFM imaging with functionalized tips. *Phys. Rev. B* **90**, 085421 (2014).
29. Zhu, C. et al. Direct observation of two-dimensional ices on different surfaces near room temperature without confinement. *Proc. Natl Acad. Sci. USA* **116**, 16723–16728 (2019).
30. Gerrard, N. et al. Strain relief during ice growth on a hexagonal template. *J. Am. Chem. Soc.* **141**, 8599–8607 (2019).

Methods

STM and AFM experiments

All the experiments were performed with a combined noncontact AFM/STM system (Createc) at 5 K using a qPlus sensor equipped with a tungsten tip (parameters: spring constant, $k_0 \approx 1{,}800$ N m^{-1}; resonance frequency, $f_0 = 26.7$ kHz; quality factor, $Q \approx 45{,}000$). Ultrapure H_2O (deuterium-depleted, ≤1 ppm; Sigma Aldrich) was used and further purified under vacuum by 3–5 freeze-and-pump cycles to remove remaining gas impurities. Then H_2O molecules were dosed in situ onto a clean Au(111) surface held at 120 K through a dosing tube. The as-grown sample was first checked by STM at 77 K, and then quickly cooled down to 5 K for further STM and AFM measurements. Throughout the experiments, bias voltage refers to the sample voltage with respect to the tip. The STM topographic images and AFM frequency-shift (Δf) images were obtained with the CO-terminated tips in constant-current and constant-height modes, respectively. The CO tip was obtained by positioning the tip over a CO molecule on the Au(111) surface at a set point of 100 mV and 30 pA, followed by increasing the bias voltage to 300 mV. The oscillation amplitude of experimental AFM imaging is 100 pm if not specifically mentioned.

DFT calculations

DFT calculations were performed using the Vienna Ab initio Simulation Package (VASP version 5.3)[31,32]. Projector-augmented wave pseudopotentials were used with a cutoff energy of 550 eV for the expansion of the electronic wave functions[33]. Van der Waals corrections for dispersion forces were considered using the 'optB86b-vdW' functional[34,35]. In the DFT calculations, the system consisted of the hexagonal 2D bilayer ice on top of a Au(111) substrate modelled by a four-layer slab. The lattice constant for Au was set to be 4.078 Å and the bottom three-layer Au substrate was fixed in the DFT calculations. Monkhorst–Pack k-point meshes of spacing denser than $2\pi \times 0.058$ Å^{-1} were used and the thickness of the vacuum slab was larger than 13 Å. The geometry optimizations were performed with a force criterion of 0.01 eV Å^{-1}.

Simulations of AFM images

The Δf images were simulated with a molecular-mechanics model based on methods described previously[28,36]. We used the following parameters for the probe-particle–tip model: effective lateral stiffness, $k = 0.75$ N m^{-1}; atomic radius, $R_c = 1.661$ Å. A quadrupole-like (d_{z^2}) charge distribution at the tip apex was used to simulate the CO tip[12] with $q = -0.25e$. d_{z^2} represents the atomic-orbital function used to simulate the spatial distribution of charge density at the tip apex, d is the atomic orbit, z is the orientation of the orbit, e is the elementary charge and q is the magnitude of the quadrupole charge at the tip apex. The electrostatic potentials of the ice on Au(111) used in the AFM simulations were obtained from DFT calculations. The Lennard-Jones parameters for O and H atoms in the AFM simulation were: $r_H = 1.487$ Å, $\varepsilon_H = 0.680$ meV, $r_O = 1.661$ Å and $\varepsilon_O = 9.106$ meV.

Molecular-dynamics simulations

We performed large-scale molecular-dynamics simulations and used the monoatomic model for water–water interactions[37], which consists of short-ranged two-body and three-body non-bonding potentials without explicitly including hydrogen atoms[37,38]. The 12-6 Lennard-Jones potential was used for the interaction between water and the Au atoms of the Au(111) surface. The Lennard-Jones parameters were determined to be $\varepsilon_{Au-wat} = 1.553$ kJ mol^{-1} and $\sigma_{Au-wat} = 3.2$ Å to match the experimentally measured contact angles for a water droplet on the Au(111) surface[39]. A cutoff of 10 Å was used for the Lennard-Jones potential. The velocity Verlet algorithm was used to integrate the equations of the motion with a time step of 2 fs. Periodic boundary conditions were applied in all three directions of the simulation box. All molecular-dynamics simulations were carried out using the Large-scale Atomic/Molecular Massively Parallel Simulator (LAMMPS) package[40].

We performed deposition simulations of water vapour on the Au(111) surface at 120 K. The deposition was initiated on a bare Au sheet with an area of 155.72 Å × 159.832 Å consisting of three atomic layers. The simulations were performed in a constant-volume and constant-temperature (*NVT*) ensemble. The temperature was controlled by a Langevin thermostat with a relaxation time of 1 ps. The Au sheet was kept rigid during the molecular-dynamics simulations, and the water molecules—initially located 20–25 Å above the Au surface—were given initial velocities with a random magnitude from 5.0 to 10.0 Å ps^{-1} in the direction towards the Au surface. First, we introduced one water molecule to the simulation cell every 0.3 ns. Next, more detailed molecular-dynamics simulations were performed to explore the growth behaviour of the bilayer ice at the zigzag and armchair edges, after the larger-sized bilayer ice grains were formed. For these more detailed simulations, one water molecule was introduced to the simulation cell every 100 ns at either the zigzag edge or the armchair edge. The water molecules were placed at a random initial location with a distance of 3 Å from the nearest water molecule at the edge.

The mechanism of submolecular-resolution AFM imaging

In refs. [7,27], the electrostatic forces of the individual water clusters give rise to dark features at the position of H atoms at large tip heights. However, for 2D bilayer ice at large tip heights, the long-range attractive van der Waals background of the extended water network (Extended Data Fig. 3c, green line) smears out the dark contrast of the H atoms (Extended Data Fig. 3a, z_1 in Extended Data Fig. 3c). Instead, we found that the O–H directionality imaging of the 2D ice can be achieved at smaller tip heights (z_2 in Extended Data Fig. 3c), where the Pauli repulsive forces start to set in, such that the total force signals of the water molecules are separated out from the van der Waals background (Extended Data Fig. 3b). Such an imaging mechanism relies on the delicate interplay between the higher-order electrostatic forces and Pauli repulsion forces. The contribution from the electrostatic force of H and O atoms (Extended Data Fig. 3g) can spatially modulate the Δf contrast of the Pauli repulsions, leading to the apparent O–H directionality.

To confirm the role of the higher-order electrostatic force in the AFM images, we performed systematic AFM image simulations for the 2D bilayer ice using quadrupole (d_{z^2}) (Extended Data Fig. 3d) and neutral (Extended Data Fig. 3e) tip apexes at different tip heights. The O atoms of the flat water molecules are about 1–2 pm higher than those of the vertical water molecules. At a large tip height, the vertical water molecules exhibit brighter contrast than the flat water molecules with the d_{z^2} tip (Extended Data Fig. 3d, left), and the brighter features correspond to the flat molecules for neutral tip (Extended Data Fig. 3e, left).

When the tip height was set to an intermediate value at which the higher-order electrostatic and Pauli repulsion forces are comparable, the O–H directionality of the water molecule is evident in the simulated AFM images with the d_{z^2} tip (Extended Data Fig. 3d, middle). However, such submolecular features are much less obvious when using the neutral tip (Extended Data Fig. 3e, middle). Therefore, the inclusion of the higher-order electrostatic force (d_{z^2} tip) is essential to reproduce the experimental AFM contrasts (Extended Data Fig. 3b). At a smaller tip height, where the AFM signals are dominated by the Pauli repulsion[12], the simulated AFM images show the same honeycomb structure of the 2D ice for both the neutral and d_{z^2} tips (Extended Data Fig. 3d, e, right).

To further justify the importance of the d_{z^2} tip in reproducing the experimental results, we compare the experimental and simulated force curves in Extended Data Fig. 3i–k. We note that the dip in the experimental force curve (F_z) of the flat water molecules is deeper than that of the vertical water molecules (Extended Data Fig. 3i), which cannot be explained by the simple picture based on the height difference of the flat and vertical water molecules. Instead, such a difference can be attributed to the fact that the negatively charged tip apex gains a

larger (or smaller) attractive (or repulsive) electrostatic force above the flat water molecules than that above the vertical molecules (see Extended Data Fig. 3g, j). By contrast, the neutral tip yields negligible difference in F_z curve at the dip position (Extended Data Fig. 3k). In addition, we found a crossover behaviour at small tip heights where the Pauli repulsion force is dominant (black ellipse in Extended Data Fig. 3i), which is also reproduced nicely by the d_{z^2} tip (black ellipse in Extended Data Fig. 3j) but is absent when the neutral tip is used (Extended Data Fig. 3k). This crossover behaviour results from the strong deflection of the CO tip by the Pauli repulsion force (see the red and blue arrows in Extended Data Fig. 3l). The relaxation of the CO molecule occurs earlier at the vertical water molecules than at the flat molecules, primarily arising from the different shapes of the potential surface (Extended Data Fig. 3h), where the potential distribution above the vertical water molecules appears to be more anisotropic than above the flat water molecules.

DFT-calculated formation energies of different edges of the 2D ice

To compare the relative stability of the zigzag and armchair edges, edge-formation energies (E_f) were calculated using DFT, which revealed that the unreconstructed zigzag edge and reconstructed 5756-type armchair edge are the most stable edges. The edge-formation energy[41] is defined as

$$E_f = (n_e \times E'_{ad,i} - E_{ad,e})/l$$

where n_e is the number of the water molecules in edged bilayer ice, l (in nanometres) is the length along the ice edge, and $E'_{ad,i}$ and $E_{ad,e}$, defined in Eqs. (1a) and (1b) below, are the adsorption energy (per water molecule) of the infinite 2D bilayer ice on the Au substrate and the adsorption energy of the edged 2D bilayer ice on the Au substrate, respectively.

$$E'_{ad,i} = (E[\mathrm{Au}] + n_i \times E[(\mathrm{H_2O})_g] - E[\mathrm{ice_i/Au}])/n_i \quad (1a)$$

$$E_{ad,e} = E[\mathrm{Au}] + n_e \times E[(\mathrm{H_2O})_g] - E[\mathrm{ice_e/Au}] \quad (1b)$$

where n_i is the number of the water molecules in the infinite ice, E[Au] is the energy of the bare Au substrate, $E[(\mathrm{H_2O})_g]$ is the energy of the isolated water molecule in the gas phase, and $E[\mathrm{ice_i/Au}]$ and $E[\mathrm{ice_e/Au}]$ are the total energies of the Au-supported infinite and edged 2D ices, respectively.

There are three different orientations for zigzag edges (ZZ1, ZZ2 and ZZ3) and armchair edges (AC1, AC2, and AC3), given a specific type of proton ordering (Extended Data Fig. 4a). ZZ1 and ZZ3 are equivalent, as are AC1 and AC3. Each orientation can produce two types of proton order along the edge. Experimentally, it is difficult to discern the O–H directionality at the edges because the vertical relaxation of the water molecules at the edges can easily smear out the weak-force contrasts arising from the O–H directionality. However, we could determine that the dangling OH is disfavoured at the edge of the top water layer.

We thus only performed calculations of the non-equivalent orientations for zigzag edges (Extended Data Fig. 4b, c) and armchair edges (Extended Data Fig. 4d, e) without or with fewer dangling OHs. In our calculations, one edge of the bilayer ice (orange O atoms in Extended Data Fig. 4b–e), was fixed at the same position of the infinite bilayer ice. Therefore, the relative formation energies of the other edge, ΔE_f, can be calculated after structural relaxation. Extended Data Fig. 4f shows ΔE_f with respect to the corresponding unreconstructed 6666-type zigzag and armchair edges, where the unreconstructed zigzag edge and 5756-type armchair edge are the most stable edges no matter which type of edge is considered. We note that the 6666-type armchair edge cannot be seen in the experiment, although the energy of the 6666-type edge is smaller than that of the 5656-type edge. This is due to the existence of a stable composite 575/656 structure (t = 0.4 μs in Fig. 4b), which considerably lowers the 5756-to-5656 conversion barrier (see Extended Data Fig. 9). Therefore, the growth of armchair edges is governed by the interplay between the thermodynamics and kinetics, leading to the 5756-to-5656 conversion in the absence of a 6666-type edge.

Insight into the stability of the zigzag and armchair edges

To gain further insight into the formation energies of different edges, we decomposed the DFT-calculated formation energy E_f into three parts: the energy difference between the edged state and infinite state of the Au(111) substrate, $E_{f,Au}$, the ice, $E_{f,ice}$, and the interaction between the Au(111) substrate and the ice, $E_{f,Au-ice}$. We found that $E_{f,Au}$ is negligible, and thus the only noticeable contributions to E_f are from $E_{f,ice}$ and $E_{f,Au-ice}$. The detailed relative energies (ΔE) with respect to the energy of the corresponding unreconstructed 6666-type edge are shown in Extended Data Fig. 5a, b, where the cyan, blue and red bars represent $\Delta E_{f,Au-ice}$, $\Delta E_{f,ice}$ and ΔE_f, respectively. In particular, we found that $\Delta E_{f,ice}$ is the dominant component of ΔE_f, which largely determines the relative stability of different ice edges.

The three parts of the formation energy E_f are defined as

$$E_{f,Au} = (E[\mathrm{Au_e}] - E[\mathrm{Au_i}])/l \quad (2)$$

$$E_{f,ice} = (E[\mathrm{ice_e}] - n_e \times E[\mathrm{ice_i}]/n_i)/l \quad (3)$$

$$E_{f,Au-ice} = (E[\mathrm{ice_e/Au}] - E[\mathrm{ice_e}] - E[\mathrm{Au_e}] - n_e \times E'_{Au-ice})/l \quad (4)$$

The E'_{Au-ice} is the binding energy (per water molecule) between the Au(111) substrate and the infinite 2D ice, defined in Eq. (5)

$$E'_{Au-ice} = (E[\mathrm{ice_i/Au}] - E[\mathrm{ice_i}] - E[\mathrm{Au_i}])/n_i \quad (5)$$

where $E[\mathrm{Au_e}]$ and $E[\mathrm{ice_e}]$ are the energies of the Au substrate and the ice separated from the Au-supported edged ice, respectively; $E[\mathrm{Au_i}]$ and $E[\mathrm{ice_i}]$ are the energies of the Au substrate and the ice separated from the Au-supported infinite ice, respectively.

To explore the reason why the armchair edge is reconstructed to the 5756-type edge, we analysed some details of H bonds at different armchair edges in DFT calculation. $\Delta E_{f,ice}$ is mainly related to the H-bonding interaction between the water molecules at the ice edge. We note on one hand that the density of unsaturated H bonds at the 5756-type armchair edge is reduced from that of the unreconstructed 6666-type ($1.15/a_{ice}$) to $0.87/a_{ice}$, which can greatly lower the formation energy of the armchair edge. On the other hand, the formation of the 5756-type armchair edge introduces only a very small strain on the H bonds, as suggested by the small deviation of H-bonding length and angles from the unreconstructed 6666-type (Extended Data Fig. 5c). Therefore, the 5756-type armchair edge should be energetically favoured over the unreconstructed 6666-type.

Although the 5656-type edge has an even smaller density of unsaturated H bonds ($0.58/a_{ice}$) than does the 5756-type edge, it is much more stressed (Extended Data Fig. 5c) and becomes less stable than the 5756-type edge. Indeed, we found by experiment that the length of the 5656-type edges is primarily below 10 Å, which is considerably shorter than that of the 5756-type edges (Extended Data Fig. 5d). Such a difference can be explained by considering that the 5656-type edge cannot grow too long, owing to the accumulation of strain energy. Therefore, the stabilization of the 5756-type armchair edge results from the combined effects of minimizing the unsaturated H bonds and reducing the strain energy.

Stability of various intermediate structures at the edges obtained by molecular-dynamics simulations

We note that some intermediate structures in molecular-dynamics simulations shown in Fig. 4 cannot be observed in experiments (Fig. 3).

This is related to the relative stability and lifetime of the various intermediate structures. Owing to computational limitations, it is very difficult to obtain the accurate lifetimes for the intermediate structures, which are relatively long compared to the simulation time. Instead, we have calculated the interacting energy (ΔE_b) between a water molecule at the edge and the remaining water molecules together with the Au substrate after optimization for various intermediate structures by classical force field. The maximum interacting energy corresponds to that needed to decompose the existing structure during the growth, thus providing an estimation for the lifetime.

As shown in Extended Data Fig. 9, our calculations show that the maximum interacting energy between a water molecule at the zigzag edge and the remaining water molecules follows ZZ3 > ZZ2 > ZZ4 > ZZ5 > ZZ6 > ZZ1. Such a trend suggests that individual pentagon structures attached at the zigzag edge (ZZ1) are the most stable. By contrast, zigzag-565 (ZZ4) should have the shortest lifetime among the intermediate structures with paired water, which explains why such a structure cannot be observed experimentally. In addition, we note that the lifetime of the 5(6···6)5 structure at the zigzag edge increases with the number of the hexagons.

For armchair edge structures, the maximum interacting energy follows AC4 > AC3 > AC2 > AC1. Interestingly, it was revealed that the composite 575/656 structure (AC1) is very stable. However, we cannot distinguish between the 575/656 structure and the 5756-type edge in experiment, because only the top layer of the 2D bilayer ice can be imaged by STM and AFM. Such a composite 575/656 structure would greatly facilitate the 5756-to-5656 conversion during the growth of the armchair edge structure. Furthermore, the lifetime of the 5656-type edge decreases rapidly as its length increases, which is consistent with experimental results that indicate that the observed 5656-type edges are mostly short.

Data availability

The source data are available from the corresponding authors upon reasonable request.

Code availability

The custom code and mathematical algorithms that support the findings of this study are available from the corresponding authors upon reasonable request.

31. Kresse, G. & Hafner, J. Ab initio molecular dynamics for liquid metals. *Phys. Rev. B* **47**, 558–561 (1993).
32. Kresse, G. & Furthmuller, J. Efficient iterative schemes for ab initio total-energy calculations using a plane-wave basis set. *Phys. Rev. B* **54**, 11169–11186 (1996).
33. Kresse, G. & Joubert, D. From ultrasoft pseudopotentials to the projector augmented-wave method. *Phys. Rev. B* **59**, 1758–1775 (1999).
34. Klimeš, J., Bowler, D. R. & Michaelides, A. Chemical accuracy for the van der Waals density functional. *J. Phys. Condens. Matter* **22**, 022201 (2010).
35. Klimeš, J., Bowler, D. R. & Michaelides, A. van der Waals density functionals applied to solids. *Phys. Rev. B* **83**, 195131 (2011).
36. Hapala, P., Temirov, R., Tautz, F. S. & Jelinek, P. Origin of high-resolution IETS-STM images of organic molecules with functionalized tips. *Phys. Rev. Lett.* **113**, 226101 (2014).
37. Molinero, V. & Moore, E. B. Water modeled as an intermediate element between carbon and silicon. *J. Phys. Chem. B* **113**, 4008–4016 (2009).
38. Lupi, L. et al. Role of stacking disorder in ice nucleation. *Nature* **551**, 218–222 (2017).
39. Erb, R. A. Wettability of gold. *J. Phys. Chem.* **72**, 2412–2417 (1968).
40. Plimpton, S. Fast parallel algorithms for short-range molecular dynamics. *J. Comput. Phys.* **117**, 1–19 (1995).
41. Gao, J. F., Zhao, J. J. & Ding, F. Transition metal surface passivation induced graphene edge reconstruction. *J. Am. Chem. Soc.* **134**, 6204–6209 (2012).
42. Sader, J. E. & Jarvis, S. P. Accurate formulas for interaction force and energy in frequency modulation force spectroscopy. *Appl. Phys. Lett.* **84**, 1801–1803 (2004).
43. Li, X. Z., Walker, B. & Michaelides, A. Quantum nature of the hydrogen bond. *Proc. Natl Acad. Sci. USA* **108**, 6369–6373 (2011).

Acknowledgements We thank J.-J. Wang for discussions. This work was supported by the National Key R&D Program under grant numbers 2016YFA0300901, 2017YFA0205003 and 2015CB856801, the National Natural Science Foundation of China under grant numbers 11888101, 11634001, 21725302 and 11525520, the Strategic Priority Research Program of the Chinese Academy of Sciences under grant number XDB28000000, and the Beijing Municipal Science & Technology Commission. J.S.F. and X.C.Z were supported by US National Science Foundation (CHE-1665324). We are grateful for the computational resources provided by the TianHe-1A and TianHe II supercomputers, by the High-performance Computing Platform of Peking University supercomputing facility, and by the UNL Holland Computing Center.

Author contributions Y.J. and E.-G.W. designed and supervised the project. R.M. and Y.T. performed the STM/AFM measurements with J.G. and J.P.; D.C., J.C., X.-Z.L. and L.-M.X. performed ab initio DFT calculations. C.Z., J.S.F. and X.C.Z. carried out the classical molecular-dynamics simulations. D.C. carried out the theoretical simulations of the AFM images. R.M., D.C., C.Z., Y.T., J.C., X.-Z.L., X.C.Z., L.-M.X., E.-G.W., and Y.J. analysed the data. Y.J., R.M., D.C., L.-M.X., C.Z. and X.C.Z. wrote the manuscript with the input of all other authors. The manuscript reflects the contributions of all authors.

Competing interests The authors declare no competing interests.

Additional information
Supplementary information is available for this paper at https://doi.org/10.1038/s41586-019-1853-4.
Correspondence and requests for materials should be addressed to X.C.Z., L.-M.X., E.-G.W. or Y.J.
Peer review information *Nature* thanks Miquel Salmeron and Yoshiaki Sugimoto for their contribution to the peer review of this work.
Reprints and permissions information is available at http://www.nature.com/reprints.

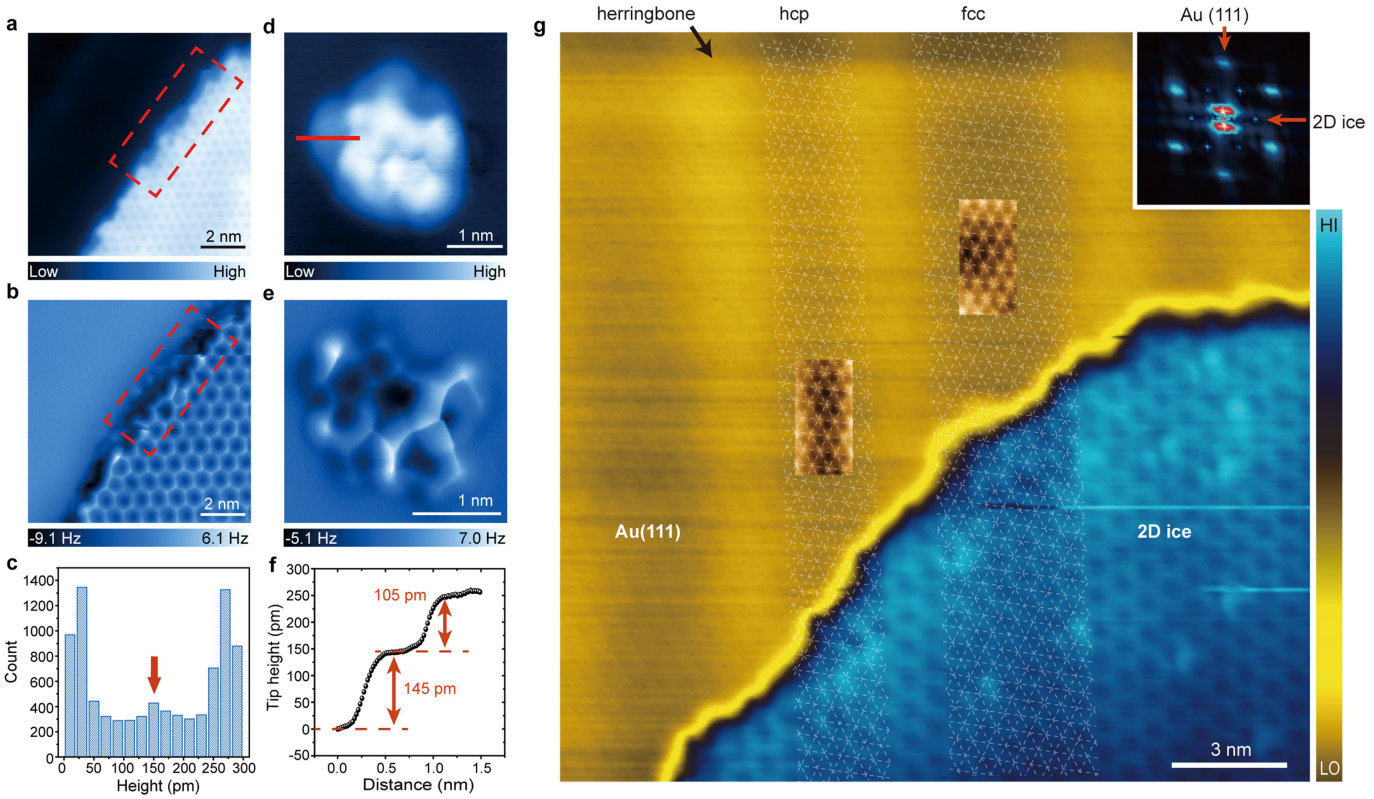

Extended Data Fig. 1 | Experimental evidence for the bilayer nature of 2D ice. **a**, **d**, STM images of a bilayer ice island (**a**) and cluster (**b**). Set point, 100 mV and 10 pA. **b**, **e**, AFM images of the same ice island (**b**) and cluster (**e**). **b** was acquired at the constant-current mode with set point 100 mV and 50 pA. **e** was recorded at a constant height of 280 pm, referenced to the set point of 100 mV and 50 pA on the Au(111) substrate. **c**, Height-distribution diagram within the red dashed rectangular area in **a**. The red arrow denotes the bottom layer of the bilayer ice, proving the bilayer nature of the 2D ice. **f**, Height profile across the red line shown in **d**, giving two different steps with heights of about 150 pm and about 250 pm, consistent with the results of the 2D ice island. **g**, False-colour STM image of a 2D ice island grown on a Au(111) surface, where the honeycomb structure of the 2D ice and the herringbone reconstruction of the Au(111) surface are distinguishable. The atomically resolved STM images of the Au(111) lattice are superimposed within the face-centred cubic (fcc) and hexagonal close-packed (hcp) regions, showing good registry between the 2D ice and the Au substrate. The set points are 100 mV and 10 pA and 5 mV and 6 nA for the ice island and the Au(111) lattice, respectively. The white dashed grids correspond to the 1×1 lattice of Au(111) within the fcc and hcp regions. The inset at the upper-right corner is a composite 2D-FFT image of the Au(111) and 2D-ice lattice, and shows the corresponding 1×1 and $\sqrt{3} \times \sqrt{3}$ periodicities.

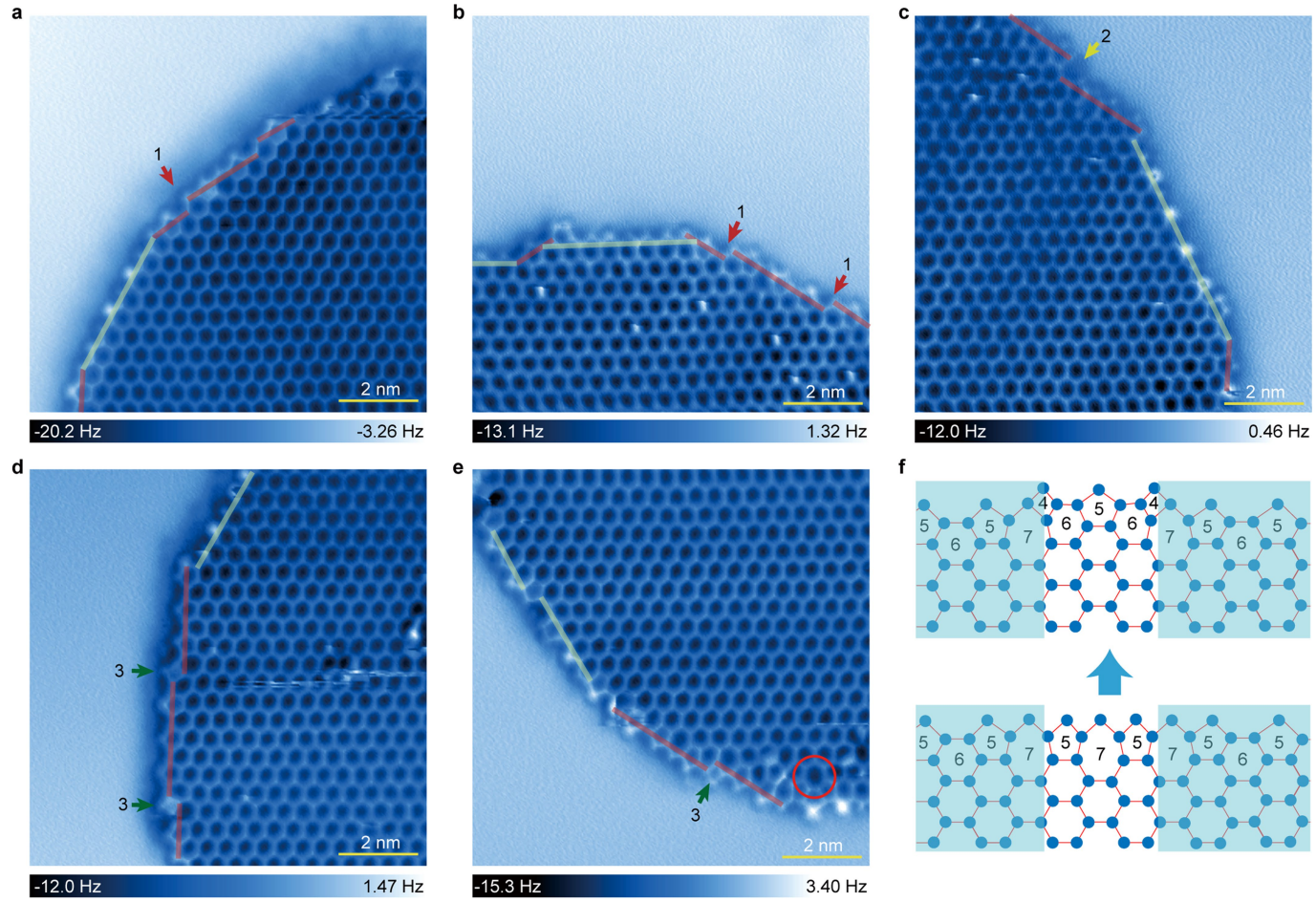

Extended Data Fig. 2 | Interruption of the armchair edges by defects and kinks. a–**e**, Constant-height AFM images of edge areas that contain short reconstructed armchair edges. The tip height is $z_{offset} = -10$ pm, referenced to the STM set point 100 mV and 50 pA on the water molecules of the second layer of bilayer ice. The red and green lines represent the armchair and zigzag edges, respectively. The red, green and yellow arrows point to three types of kinks at the armchair edges. Type-1 (red) and type-2 (yellow) kinks correspond to the cases where the armchair edges are terminated at the hexagons and pentagons, respectively. The local seeding growth model requires individual nucleation centres to facilitate the growth of the armchair edges, naturally leading to these step-like structures. **f**, Schematic showing the formation of type-3 (green arrows) kink defects, consisting of 647-type member rings. These defects are formed owing to the position of the heptagons at the armchair edges, which leads to two different structure series. The green shaded areas represent 5657-member-ring series, and the unshaded areas represent the 5756-type member ring series. The joint of the two different series results in a type-3 defect, which could further develop into a trapped 7-type member ring in the second-outermost layer, as indicated by a red circle in **e**.

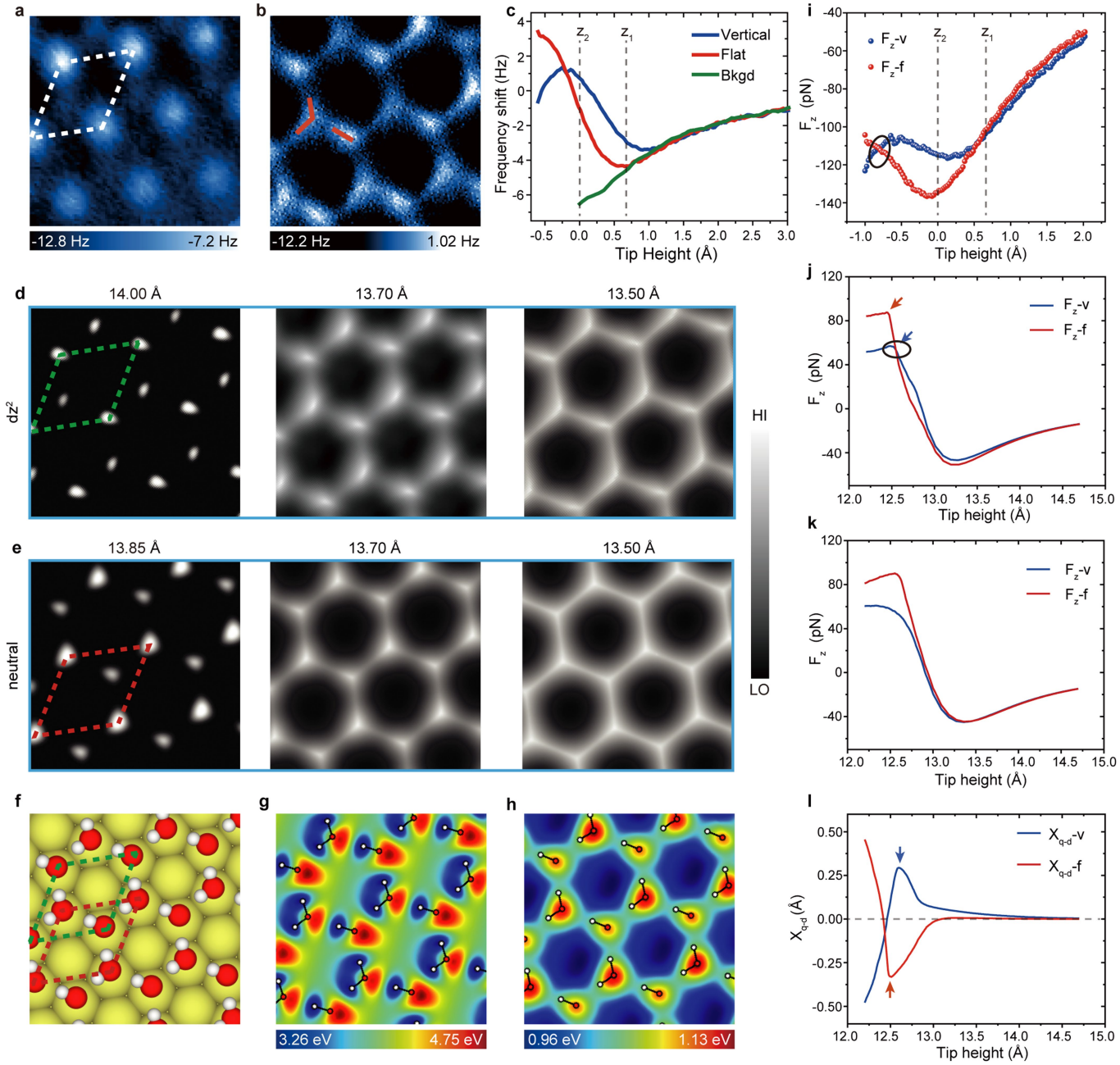

Extended Data Fig. 3 | The mechanism of submolecular-resolution AFM imaging. a, **b**, Experimental AFM frequency-shift (Δf) images obtained at tip heights and oscillation amplitudes of 70 pm and 40 pm (**a**) and 0 pm and 100 pm (**b**). **c**, Δf curves (oscillation amplitude, 40 pm) above a vertical water molecule (vertical), a flat molecule (flat) and the hollow site of hexagonal ice lattice (denoted as background, bkgd) as a function of the tip height. z_1 and z_2 denote the tip heights of the two Δf images in **a** and **b**, respectively. **d**, **e**, Simulated Δf images at different tip heights z (given above each image) obtained with quadrupole (d_{z^2}, $q = -0.25e$; **d**) and neutral ($q = 0$; **e**) tips. **f**, Top view of the 2D bilayer ice structure (top layer) on the Au(111) substrate. The bottom ice layer is hidden to highlight the structure of the top layer. The green and red dashed parallelograms in **d**–**f** denote the sub-lattices of the vertical and flat water molecules, respectively. **g**, Calculated electrostatic potential map of the bilayer ice on the Au(111) in a plane 7.24 Å above the highest atom in the Au substrate. **h**, Simulated total potential map of the bilayer ice on Au(111) in a plane, corresponding to the position of the CO-tip apex at a tip height of 12.5 Å. **i**–**k**, Vertical force above the flat ($F_{z\text{-}f}$) and vertical ($F_{z\text{-}v}$) water molecule as a function of tip height. **i**, Experimental F_z obtained by integrating the experimental $\Delta f(z)$ in **c** according to ref. [42]. Before the integration, $\Delta f(z)$ was smoothed using a moving average filter with a span of 5. **j**, **k**, Simulated F_z computed with d_{z^2} (**j**) and neutral (**k**) tips. **l**, Simulated lateral deflection of the quadrupole probe particle in the x direction ($X_{q\text{-}d}$) as a function of the tip height. $X_{q\text{-}d\text{-}v}$ and $X_{q\text{-}d\text{-}f}$ correspond to $X_{q\text{-}d}$ above the vertical water molecule and the flat water molecule, respectively. Tip-height references are the same as those in Fig. 2. In **g** and **h**, H and O atoms in the top-layer ice are denoted as white and red spheres, respectively. The image sizes in **a**, **b** and **d**–**h** are 1.25 nm × 1.25 nm. See Methods for details.

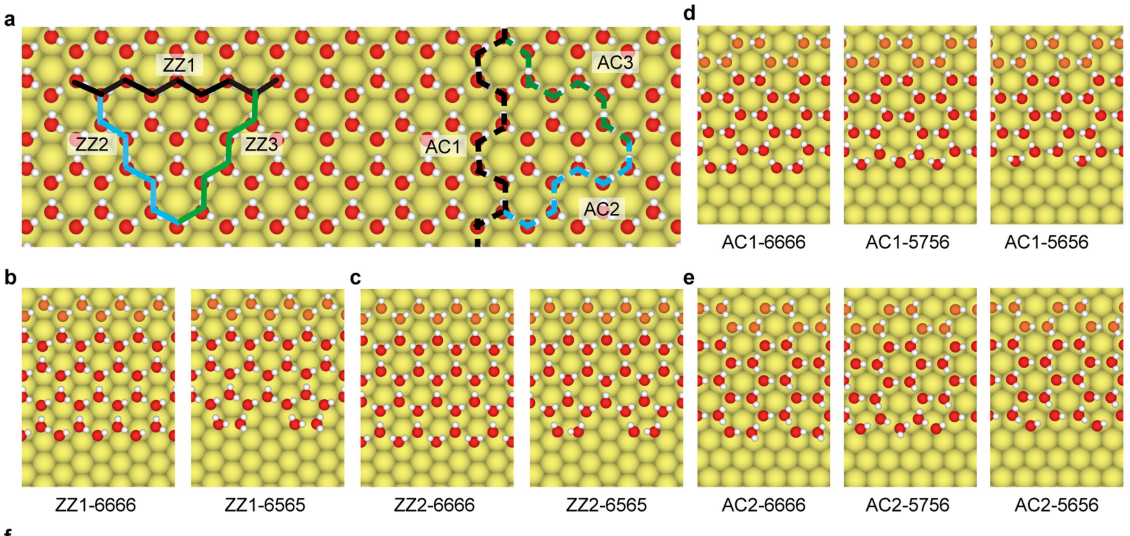

f

ΔE_f (meV/nm)	Zigzag edge (ZZ)		Armchair edge (AC)		
	6666	6565	6666	5756	5656
Type 1	0	127	0	-105	109
Type 2	0	75	0	-28	179

Extended Data Fig. 4 | DFT-calculated formation energies of different edges of the 2D ice. a–**e**,Top view of the top layer of bulk (**a**), zigzag (ZZ)-edged (**b**, **c**), and armchair (AC)-edged (**d**, **e**) 2D ices on a Au(111) substrate. The three different zigzag and armchair edge type are denoted in **a** by solid and dashed poly lines, respectively. The fixed edges during the structural relaxation are marked in orange. The bottom ice layer is hidden, to highlight the structure of the top layer. Image sizes: 6.52 nm × 2.17 nm (**a**), 2.00 nm × 2.61 nm (**b**, **c**), and 1.73 nm × 2.61 nm (**d**, **e**). Lateral size of the supercell used in the DFT calculations: 2.00 nm × 3.46 nm (**b**, **c**) and 1.73 nm × 3.50 nm (**d**, **e**). **f**, The relative formation energy (ΔE_f) of the different edge types. See Methods for details.

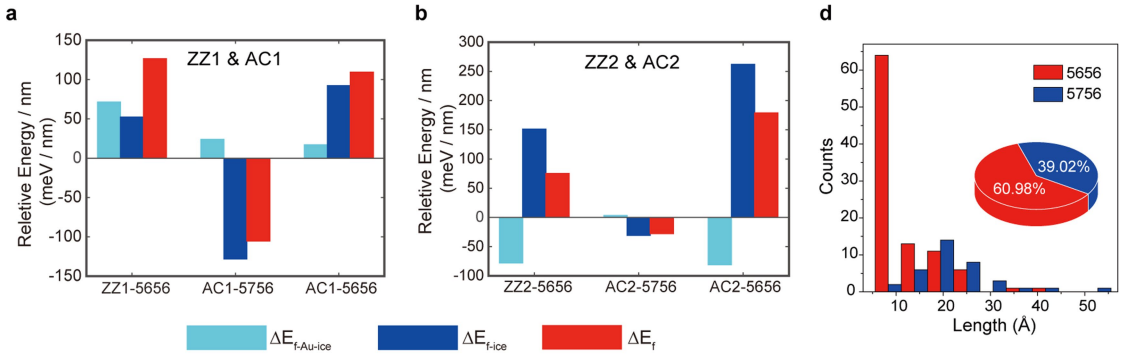

c

Armchair edge	d_{OO} (Å)			O-H…O angel (°)		
	6666	5756	5656	6666	5756	5656
AC1	2.756	2.781	2.945	165.489	165.860	162.311
AC2	2.761	2.771	2.934	165.960	165.326	163.081

Extended Data Fig. 5 | Insight into the stability of the zigzag and armchair edges. a, **b**, Decomposed DFT-calculated relative formation energies of the 2D bilayer ice with different edge types (ZZ1 and AC1, **a**; ZZ2 and AC2, **b**). The relative formation energies of different edges are referenced to that of the corresponding unreconstructed 6666-type edge. The cyan, blue and red bars represent the relative energy of the interaction between the Au(111) substrate and the bilayer ice, the isolated bilayer ice, and the Au-supported bilayer ice, respectively. **c**, The average O–O distance[43] (d_{OO}) and H-bonding angle[43] (O–H…O angle) of the outermost rings of different armchair edges. **d**, Experimental length distribution diagram of 5656- and 5756-type armchair edges for ten ice islands, $n = 122$. Inset, Statistics on the total length of corresponding edges. See Methods for details.

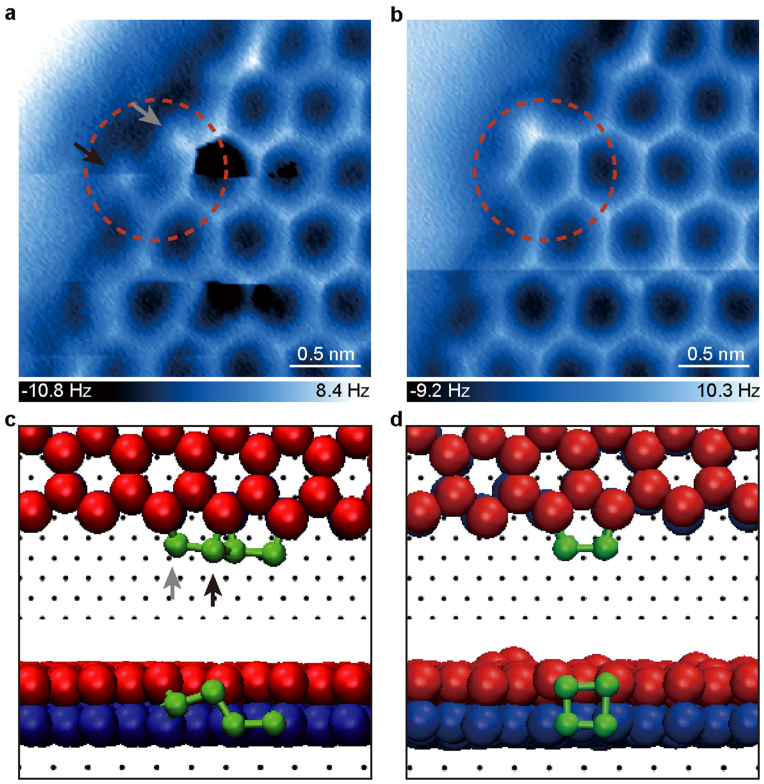

Extended Data Fig. 6 | Tip-induced growth of the pentagon structure at the zigzag edge. a, **b**, AFM images of the same area during the consecutive scanning showing the formation of the pentagon structure. Tip height, z_{offset} = −10 pm, referenced to the STM set point of 100 mV and 50 pA on the water molecule of the bilayer ice. **c**, **d**, The corresponding snapshots in the molecular-dynamics simulations. The dangling-like water molecule corresponds to the molecule attached to the top layer (see the black arrows in **a** and **c**), and the water molecule located at the middle of the bilayer ice has an apparently shorter bond (grey arrows in **a** and **c**). As highlighted by the red dashed circles in **a** and **b**, during close imaging at a very small tip height, a complete pentagon structure at the zigzag edge can be formed, induced by the perturbation of the tip.

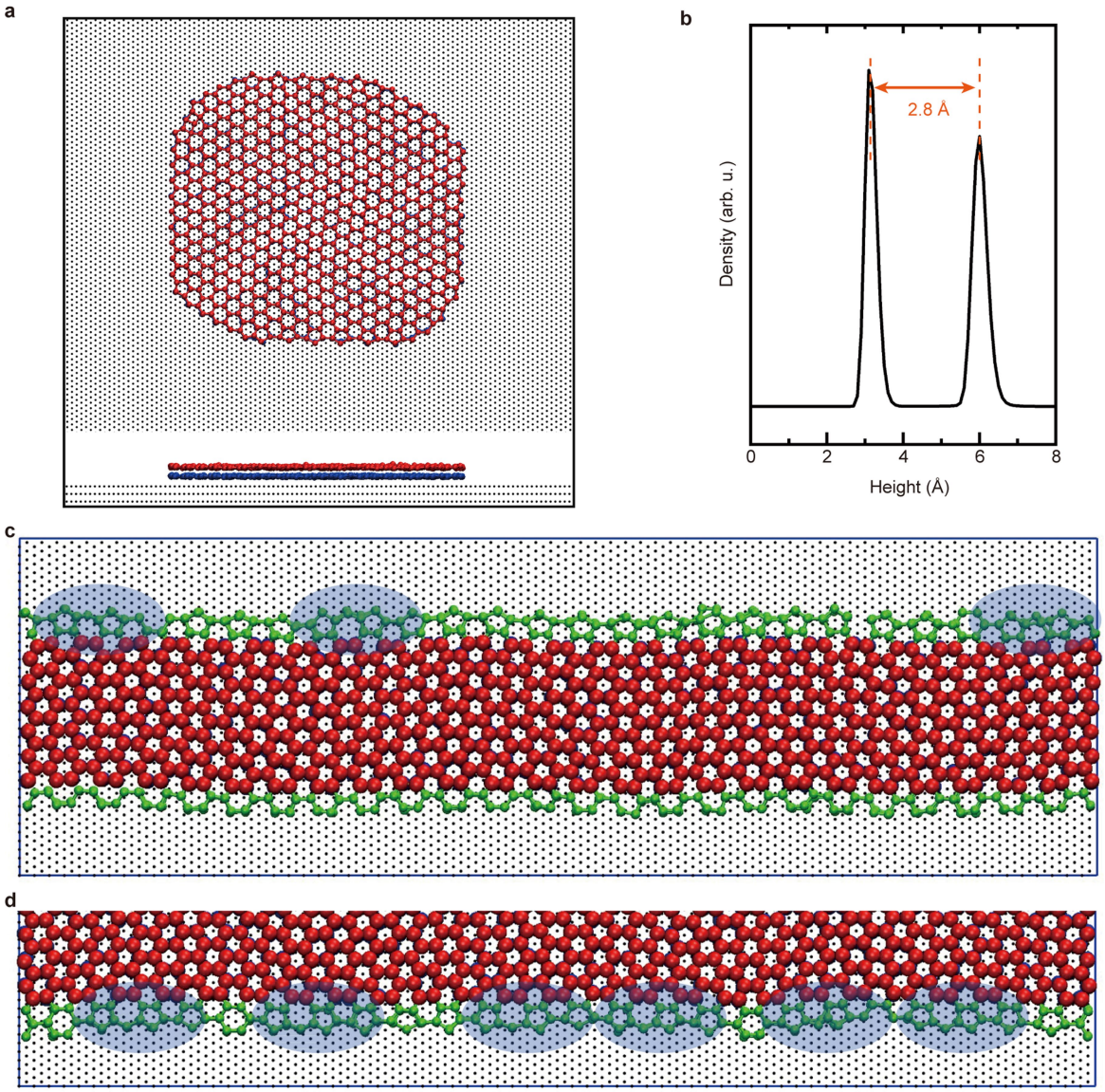

Extended Data Fig. 7 | Molecular-dynamics simulation of 2D ice formation and armchair edge stability. a, Top (upper) and side views (lower) of a snapshot show 1,394 water molecules deposited on a Au(111) surface at 120 K. The bottom layer of water molecules is shown in blue and the top layer in red. Au atoms of the Au surface are shown in black. No good registry between the 2D ice and the Au substrate is found, probably due to the weak interaction between them. Although 5656-type armchair edges appear, the 5756-type and 6666-type armchair edges are absent, because of the coincident number of the water molecules added and the limited length of the edges. **b**, Transverse density profile of the 2D bilayer ice. The intensity of the lower peak is slightly larger than that of the higher one, indicating that the growth of bilayer ice starts from the bottom layer. **c**, Snapshot of a bilayer ice ribbon (20.76 nm in length) on a Au(111) surface after relaxation for 20 ns, originally with two armchair edges of 5656-type (upper) and 6666-type (lower). Some 5656-type structures spontaneously convert to 5756-type structures (highlighted by blue ellipses) during the simulation, indicating that the 5756-type edge should be thermodynamically more stable than the 5656-type edge. **d**, Snapshot at $t = 1\,\mu s$ after 63 water molecules were introduced to 6666-type armchair edges. Most of 6666-type structures change to 5756-type or 5656-type structures, suggesting that the growth of armchair edges is governed by the 5756-to-5656 conversion in the absence of a 6666-type edge.

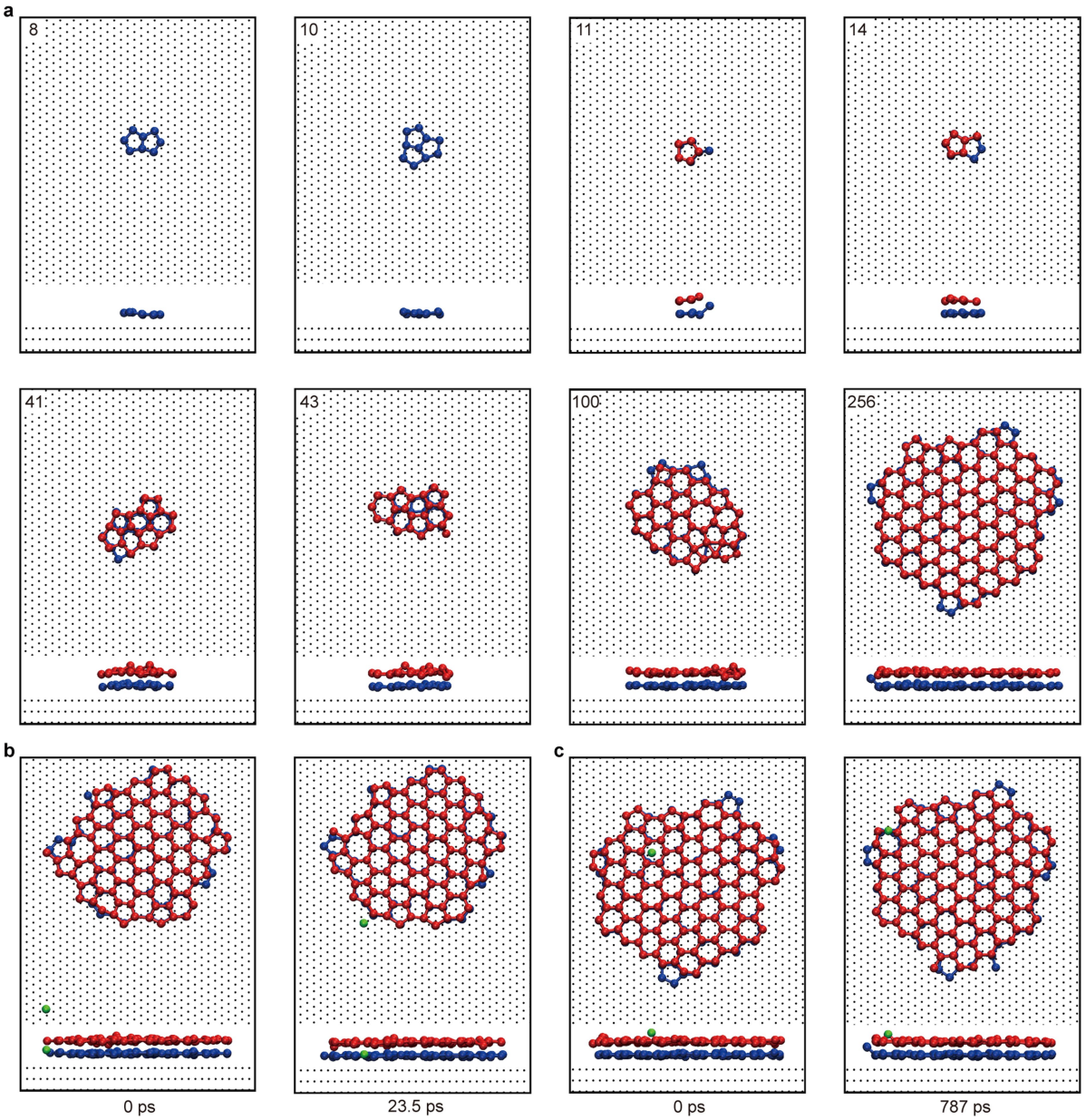

Extended Data Fig. 8 | Nucleation of the 2D ice on the Au surface. a, Top (upper) and side views (lower) of consecutive snapshots show 8, 10, 11, 14, 41, 43, 100 and 256 water molecules deposited on a Au(111) surface at 120 K. The 2D bilayer ice structure was gradually formed through single-layer and double-layer liquid clusters. **b**, Top (upper) and side views (lower) of snapshots at times $t = 0$ and 23.5 ps after the deposited water molecule (green ball) arrived at the Au surface. **c**, Top (upper) and side views (lower) of snapshots at times $t = 0$ and 787 ps after the deposited water molecule (green ball) arrived on the surface of bilayer ice. The bottom layer of water molecules is shown in blue and the top layer in red, and the Au atoms of the Au surface are shown in black. The water molecule landing on the Au or ice-island surface moves around until it finds its way to attach to the edge of the ice, without creating any new nucleation centres.

a

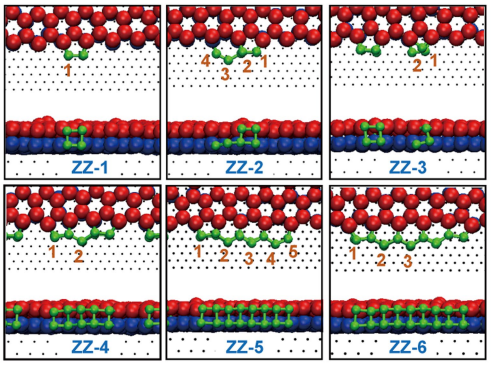

b

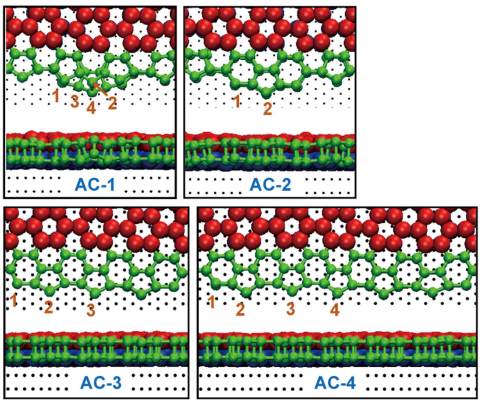

c

Zigzag edge (ZZ)					
	ZZ-1	ZZ-2			
ΔE_b (meV)	water-1	water-1	water-2	water-3	water-4
	-693.4	-686.4	-687.9	-589.1	-604.3
	ZZ-3			ZZ-4	
ΔE_b (meV)	water-1	water-2		water-1	water-2
	-530.0	-714.2		-641.5	-633.6
	ZZ-5				
ΔE_b (meV)	water-1	water-2	water-3	water-4	water-5
	-646.0	-665.0	-689.7	-694.7	-694.0
	ZZ-6				
ΔE_b (meV)	water-1		water-2		water-3
	-648.7		-660.7		-681.8
Armchair edge (AC)					
	AC-1				
ΔE_b (meV)	water-1	water-2		water-3	water-4
	-709.0	-714.0		-759.1	-725.5
	AC-2		AC-3		
ΔE_b (meV)	water-1	water-2	water-1	water-2	water-3
	-662.7	-650.7	-629.3	-651.9	-634.8
	AC-4				
ΔE_b (meV)	water-1	water-2		water-3	water-4
	-652.3	-634.4		-621.7	-599.9

Extended Data Fig. 9 | Stability of various intermediate structures at the zigzag and armchair edges obtained by molecular-dynamics simulations. **a**, **b**, Molecular-dynamics simulations snapshots of various intermediate structures during the growth of the zigzag (**a**) and armchair (**b**) edges. One water molecule was introduced to the simulation cell every 100 ns. The representative water molecules with low coordination at the edges are marked by numbers. **c**, The calculated interacting energy (ΔE_b) for the different intermediate structures shown in **a** and **b**. ΔE_b is defined as the interacting energy between a specific water molecule and the remaining water molecules together with the Au atoms in substrate after optimization. The maximum energy values are indicated in red. See Methods for details.

a

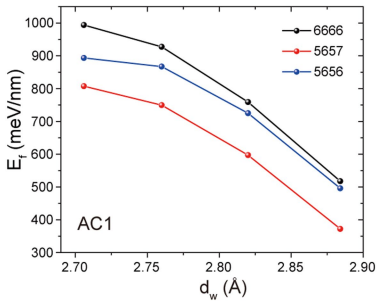

b

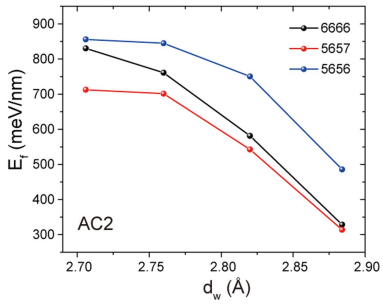

c

d(Au-Au) = 2.884 Å,d(water-water) = 2.884 Å					
ΔE_f (meV/nm)	zigzag edge		armchair edge		
	6666	6565	6666	5756	5656
	0	99.2	0	-159.5	144.2
d(Au-Au) = 2.884 Å, d(water-water) = 2.768 Å (no lattice registry)					
ΔE_f (meV/nm)	zigzag edge		armchair edge		
	6666	6565	6666	5756	5656
	0	63.8	0	-22.6	51.0
free-standing ice, d(water-water) = 2.74 Å					
ΔE_f (meV/nm)	zigzag edge		armchair edge		
	6666	6565	6666	5756	5656
	0	62.7	0	-35.4	29.1
d(Au-Au) = 2.74 Å, d(water-water) = 2.74 Å					
ΔE_f (meV/nm)	zigzag edge		armchair edge		
	6666	6565	6666	5756	5656
	0	83.6	0	-5.0	100.0

Extended Data Fig. 10 | The influence of water spacing on the stability of different edges. a, **b**, The DFT-calculated edge-formation energies as a function of water spacing (d_w) for free-standing 2D ice with different proton ordering (AC1 and AC2, see Extended Data Fig. 4a for detailed definitions). The 2D ice with minimum energy has a water spacing of 2.706 Å. The relative stability of the different armchair edges remains unchanged with water spacing from 2.706 Å to 2.884 Å; the 5756-type armchair edge is the most stable edge. The abscissa reflects the cell size in the direction parallel to the edge, which is crucial, owing to the periodic boundary conditions in the calculation. d_w corresponds to the nearest water–water spacing along the direction parallel to the edge. E_f represents the edge formation energy, similar to that defined in Methods section 'DFT-calculated formation energies of different edges of the 2D ice'. All atoms in the ice edge were fully relaxed and the structures of the different ice edges are similar as those in Extended Data Fig. 4. **c**, The relative formation energy (ΔE_f) of different edges calculated by classical force field, which follows 5656 > 6666 > 5756 for all cases, regardless of the water spacing and the commensurability with the substrate.